DFT Study of a Single *F* Center in Cubic $SrTiO_3$ Perovskite

R. A. EVARESTOV,[1] E. A. KOTOMIN,[2,3] YU. F. ZHUKOVSKII[2,3]

[1]*Department of Quantum Chemistry, St. Petersburg State University, 26 Universitetskii Prosp., Stary Petergof, 198504 St. Petersburg, Russia*

[2]*Institute of Solid State Physics, University of Latvia, 8 Kengaraga Str., LV-1063 Riga, Latvia*

[3]*Materials Research Center, Northwestern University, 2145 Sheridan Rd., Evanston, Illinois 60208, USA*

Received 21 June 2005; accepted 26 August 2005
Published online 2 November 2005 in Wiley InterScience (www.interscience.wiley.com).
DOI 10.1002/qua.20855

ABSTRACT: Various properties of a cubic phase of $SrTiO_3$ perovskite containing single *F* centers (neutral oxygen vacancies), including energies of their formation and migration, were simulated using different formalisms of density functional theory (DFT) as implemented into CRYSTAL-2003 and VASP computer codes. The lattice relaxation around the *F* center was found to be sensitive to both shape and size of supercells used. The larger the supercell, the closer the defect energy level in the bandgap lies to the conduction band bottom. It approaches the optical ionization energy of 0.49 eV for 270- and 320-atom supercells, where the distance between neighboring defects increases up to four lattice constants. The defect bandwidth decreases for these supercells down to 0.02 eV, i.e., the defect–defect interaction becomes negligible. Thus, the two different first-principles periodic approaches combined provide results that are converged with respect to the supercell size and correspond to a single defect limit. © 2005 Wiley Periodicals, Inc. Int J Quantum Chem 106: 2173–2183, 2006

Key words: periodic DFT calculations; cubic $SrTiO_3$ perovskite; *F* center; defect formation and migration; electronic properties

1. Introduction

Beneficial properties of ABO_3-type perovskite materials can be obtained by means of a deliberate deviation of oxygen content from the ideal stoichiometry, which is relevant for their numerous high-tech applications as sensors, fuel cells, microelectronic devices, etc. [1, 2]. At low partial oxygen pressure, the electric conductivity of $SrTiO_3$ perovskite is controlled by both concentration and mobility of oxygen vacancies, which act as effective donors; therefore, this material becomes *n*-type conductive [3]. Increasing the partial pressure reduces the carrier concentration, and at high pressures the conductivity goes through a minimum:

Correspondence to: Yu. F. Zhukovskii; e-mail: quantzh@latnet.lv
Contract grant sponsor: National Science Foundation.
Contract grant number: DMR-0076091.

the material becomes *p*-type [4]. Consequent thermal reduction of oxygen in a single-crystalline strontium titanate results in the insulator-to-metal transition, up to a possible superconducting state, accompanied by intensive formation of vacancies and their high density within the skin region [5].

Considerable experimental efforts were made for understanding the nature of defective strontium titanate, including the ionic transport [5, 6] and the structural properties [1, 7, 8]. The nature of the oxygen vacancy in $SrTiO_3$ perovskite was also simulated theoretically [4, 9–15]. This is very important, since modern scanning transmission electron microscopy (STEM) and reflection high-energy electron diffraction (RHEED) combined with atomic-scale electron energy-loss spectroscopy (EELS) are able to detect the presence of even single impurities and vacancies in $SrTiO_3$ [1].

Oxygen vacancies play a noticeable role in the structural transformations in bulk $SrTiO_3$, which possesses two relevant structures: the tetragonal antiferro-distortive (AFD) phase, and the cubic phase [9]. The latter (Fig. 1) is stable at >105 K, whereas AFD (slightly distorted cubic phase) is stable at lower temperatures. When simulating a single point defect, the main problem is to understand changes induced by it in the atomic and electronic structure of a host crystal. Perfect $SrTiO_3$ crystal has a mixed ionic-covalent nature of the chemical bonding, which is not in complete conformity with the formal charges on Sr^{2+}, Ti^{4+}, and O^{2-} ions. The formalism of Wannier functions applied recently for the determination of effective charges and bond populations in several perovskite crystals [16] calculated previously using the density functional theory (DFT) method [17] gives the atomic charge of +2.55 *e* on titanium and −1.55 *e* on oxygen, whereas the Ti–O bond order is 0.35 *e*; only the charge on Sr (1.95 *e*) is close to the nominal ionic value +2 *e*, confirming that strontium is ionically bonded in $SrTiO_3$. Partly covalent chemical bonding makes rather complicated simulations of the structural defects in strontium titanate, even in a cubic phase. This simplest defect may be described in terms of either neutral oxygen vacancy (single O atom removed from the lattice site) or neutral *F* center (O vacancy trapped the electron density (2–δ) *e* remaining in a host crystal). Theoretical studies mainly predict equal contributions of the 3*d* orbitals of the two nearest titanium ions (Fig. 1) into the wave function of the *F* center [4, 10–12]. According to our recent DFT calculations on a cubic phase of $SrTiO_3$ perovskite [10], the Mulliken electron charge of 1.1–1.3 *e* is localized in the neutral O vacancy (depending on the supercell size), and 0.6–0.8 *e* are equally divided by the two nearest Ti ions if we consider the *F* center. This result does not confirm formal conclusions that the *F* center is supposed to have released both electrons whereas the nearest titanium ions change their valence $Ti^{4+} \rightarrow Ti^{3+}$ [1, 4, 7].

The position of the *F* center level in the optical bandgap of $SrTiO_3$ is also not completely clear: it is an open question, whether it lies well below the conduction band bottom [12] or close to it [4, 10, 11]. The latter is supported by the indirect experimental study on the conductivity of $SrTiO_3$ ceramics, suggesting that the *F* center is a rather shallow defect [18]. Periodic ab initio calculations on the $SrTiO_3$ bulk give the values of the formation energy for O vacancy within the range of 6.5–8.5 eV [4, 9–11], whereas in cluster models [13], removal of an O atom from the lattice has a higher energy cost (>9 eV). However, this value cannot be directly measured experimentally. Conductivity in $SrTiO_3$ at low partial oxygen pressures depends on the mobility of O vacancies [3, 4, 18]. Experimental performed at high temperatures suggest an energy barrier of 0.86 eV for the *F* center diffusion in bulk [6], whereas semi-empirical pair-potential calculations on migration on the empty O vacancy result in the barriers of 0.65 eV [14] and 0.76 eV [15].

In the present work, we analyze the results of both CRYSTAL [19] and VASP [20] DFT calculations on the *F* center in a cubic phase of $SrTiO_3$ perovskite, combining advantages of LCAO and plane wave formalisms. We have optimized the lattice structural relaxation around an oxygen vacancy for supercells of different shapes and sizes. The supercells were obtained by a consequent equidistant extension of crystalline lattice vectors (Fig. 1) increasing supercell size from 80- up to 320-atom cells, in order to eliminate the interaction of periodically repeated point defects and to reach the limit of really single *F* defect. In this respect, we follow the recent study for the Fe impurities in $SrTiO_3$ [21].

2. Supercell Model of a Defective Crystal

In the first-principles band structure calculations, using the primitive unit cell in the direct space, the convergence of the bulk electronic properties (total energy per unit cell, bandgap and one-

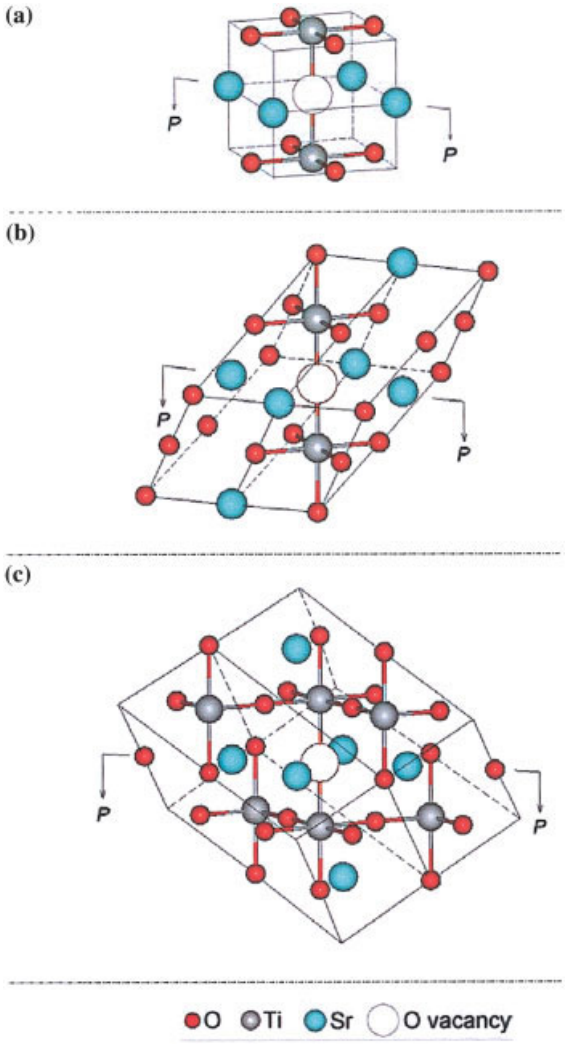

FIGURE 1. Three types of equidistant crystalline cells with a centered O vacancy for the cubic phase of $SrTiO_3$ perovskite: (a) simple cubic (sc); (b) face-centered cubic (fcc); (c) body-centered cubic (bcc). Sticks between the oxygen and titanium ions indicate the partly covalent bonds between them. To construct the difference electron density plots, each cell is sectioned along the –Ti–O–Ti– axis by the plane *P*–*P*.

electron energies of band edges, the density of states, and electronic charge distribution) can be obtained by increasing the number of ***k***-points used in the primitive Brillouin zone (BZ) [21]. The one-to-one correspondence was demonstrated [22] between the choice of ***k***-mesh and the supercell translation vectors $\{\mathbf{A}_j\}$ in a real space defined by the basic translation vectors $\mathbf{a}_i$ and primitive cell volume V_a:

$$\mathbf{A}_j = \sum_{i=1}^{3} l_{ij}\mathbf{a}_i, \tag{1a}$$

$$V_a = \mathbf{a}_1 \cdot [\mathbf{a}_2 \times \mathbf{a}_3], \tag{1b}$$

with the index $j = 1, 2, 3$. $L = \det\{l_{ij}\}$ represents a number of primitive unit cells in the corresponding supercell. Equation (1a) can be used to define the corresponding mesh $\{\boldsymbol{k}_t\}$ of the ***k***-points in the BZ [23]:

$$\exp(-i\mathbf{k}_t\mathbf{A}_j) = 1, \tag{2}$$

with indexes $j = 1, 2, 3$ and $t = 1, 2, \ldots, L$. The absolute value R_M of the smallest $\mathbf{A}_j$ in Eq. (1a) defines the accuracy of the special ***k***-points set chosen and is called cutoff length for a given ***k***-mesh [21]. Each R_M may be characterized by some number of spheres M of the basic lattice translation vectors ordered in such a way that the sphere radii are not decreasing [24]. It is possible to choose the matrix $|l_{ij}|$ in Eq. (1a), both diagonal and nondiagonal, but maintaining the point symmetry of the crystalline lattice. By increasing L, one can ensure an increase of the ***k***-mesh accuracy, and thus the accuracy of the corresponding supercell modeling of the perfect crystal. Thus, one can say that an increase of the ***k***-mesh accuracy in self-consistent band structure calculations with primitive cell means, in fact, that the perfect crystal is modeled by a sequence of supercells of the increasing size.

The use of supercell model for point defect simulation means, in fact, consideration of a "new crystal" with an artificially introduced periodicity. The point defect period is defined by a choice of supercel; the space group of a defective crystal in this model is defined by the local point symmetry of a defect and the chosen lattice of supercells [25]. A new, narrowed BZ is L-fold smaller than the original (primitive) one and may also differ by shape, when the type of lattice is changed by the transformation in Eq. (1a). The calculation of a point defect is made in the same way as for a perfect crystal using the ***k***-sampling of the BZ. In practical calculations, ***k***-sets are used, permitting minimization of the defect–defect interaction [26] for a fixed supercell size and shape. The use of the ***k***-meshes in supercell model allows one to estimate the role of defect–defect interaction through the width of the defect energy bands for each superlattice chosen: the narrower these bands, the closer the results obtained to the single defect limit. It is possible to find such a ***k***-mesh, which ensures a compromise between

the size of supercell and a reasonable reproduction of the total and one-electron energies, as well as the electron density distribution in the host crystal: the ***k***-point sets satisfying Eq. (2) are generally usually used for this purpose [21]. It is reasonable to begin from the smaller supercell containing point defect, i.e., corresponding to the converged results of the band calculations for a perfect crystal. In the specific case of the $SrTiO_3$, the initial supercell of 80 atoms was chosen. When estimating the defect–defect interaction from the calculated defect bandwidth, we make a decision about the necessity of a further increase of the supercell. As shown for the Fe impurity in $SrTiO_3$ [21], the iron bandwidth changes considerably with the supercell, increasing from 80 to 160 atoms. Comparison of the supercell results for different ***k***-meshes allows one to decide whether it is necessary to increase a supercell, in order to surpass an artificial defect–defect interaction.

The simple cubic (sc) structure of $SrTiO_3$ crystal is described mainly using the $Pm\bar{3}m$ space group [19]. In this study, the coordinate origin has been placed in O vacancy, which corresponds to the *P4/mmm* space group (Fig. 1). CRYSTAL and VASP calculations on the *F* center have been performed for the supercells of different shapes and sizes, created by a consequent equidistant extension of the lattice vectors: 80- and 270-atom face-centered cells, 135- and 320-atom simple cubic cells, as well as 160-atom body-centered cell. The corresponding sc, fcc, and bcc extensions of the $SrTiO_3$ unit cell shown in Figure 1 are described by the transformation matrices defined in Eq. (1a):

$$\begin{vmatrix} n & 0 & 0 \\ 0 & n & 0 \\ 0 & 0 & n \end{vmatrix}, \quad \begin{vmatrix} 0 & n & n \\ n & 0 & n \\ n & n & 0 \end{vmatrix} \quad \text{and} \quad \begin{vmatrix} -n & n & n \\ n & -n & n \\ n & n & -n \end{vmatrix}, \tag{3}$$

respectively, where n is varied between 2 and 4.

The length of the cube edge in the $SrTiO_3$ unit cell [Fig. 1(a)] is equal to the sc lattice constant (experimental value of 3.905 Å [9]). Strontium titanate supercells with sc extensions of $3 \times 3 \times 3$ (135 atoms) and $4 \times 4 \times 4$ (320 atoms) possess the same cubic symmetry, with a 90° angle between the lattice vectors. In turn, supercells with the fcc extensions $2\sqrt{2} \times 2\sqrt{2} \times 2\sqrt{2}$ (80 atoms) and $3\sqrt{2} \times 3\sqrt{2} \times 3\sqrt{2}$ (270 atoms) are rhombohedral with a 60° angle between the lattice vectors [Fig. 1(b)]. Lastly, for 160-atom rhombohedral bcc supercell (extension $2\sqrt{3} \times 2\sqrt{3} \times 2\sqrt{3}$), the angle is 109.47°. According to Eq. (1b), the ratio of volumes for the supercells extended from the $SrTiO_3$ unit cell using matrices, Eq. (3), with the same n is

$$V_{\text{bcc}} = 2V_{\text{fcc}} = 4V_{\text{sc}}. \tag{4}$$

For all three types of equidistant cells shown in Figure 1, their shapes correlate with the orientation of the –Ti–O–Ti– axis, it may be: (i) the rotation axis joining the centers of opposite faces [Fig. 1(a)], (ii) the diagonal joining the opposite apexes of rhombohedron [Fig. 1(b)], and (iii) the axis joining the centers of opposite rhombohedron edges [Fig. 1(c)].

3. Computational Background

3.1. CRYSTAL CALCULATIONS

The computational scheme implemented in CRYSTAL-03 code includes both Hartree–Fock (HF) and DFT ab initio methods achieved via the self-consistent field (SCF) solution of the corresponding one-electron equations [19]. The choice of the exchange-correlation functional for CRYSTAL calculations using the DFT method is an important point necessary to obtain adequate results. When modeling $SrTiO_3$ perovskite, including bulk [17] and densely packed surfaces [27], the best results were obtained using nonlocal generalized gradient approximation (GGA), combining the Becke exchange functional [28] with the correlation functional constructed by Perdew and Wang [29]. However, even this approach possesses certain shortcomings, especially when estimating the bandgap $\Delta\varepsilon_{\text{gap}}$: HF calculations markedly overestimate this value, whereas DFT calculations usually underestimate it. To avoid this artifact, the CRYSTAL-03 code [19] includes a partial incorporation of the exact HF exchange into the DFT exchange functional, with varying a mixing ratio. Thus, we have chosen the hybrid B3PW exchange-correlation functional [30] corresponding to the following energy contribution:

$$E_{xc} = (1 - a_h)\, E_x^{\text{LDA}} + a_x \Delta E_x^{\text{Becke}} + a_h E_x^{\text{HF}} + a_c \Delta E_c^{\text{PWGGA}}, \tag{5}$$

where $\Delta E_x^{\text{Becke}}$ is Becke's gradient correction to the exchange energy functional of local density E_x^{LDA} [28], E_x^{HF} is the exact HF exchange energy, $\Delta E_c^{\text{PWGGA}}$ is the gradient correction for correlation energy of Perdew–Wang [29], a_h is the input parameter of the HF/DFT exchange mixing; a_x and a_c are input pa-

TABLE I

All-electron basis set for oxygen.

Shell	Exponent (α_μ)	Contraction (c_μ) *s*	*p*	*d*
1*s*	8020.0	0.00108	—	—
	1338.0	0.00804	—	—
	255.4	0.05324	—	—
	69.22	0.1681	—	—
	23.90	0.3581	—	—
	9.264	0.3855	—	—
	3.851	0.1468	—	—
	1.212	0.0728	—	—
2*sp*	49.43	−0.00883	0.00958	—
	10.47	−0.0915	0.0696	—
	3.235	−0.0402	0.2065	—
	1.217	0.379	0.347	—
3*sp*	0.4520495	1.0	1.0	—
4*sp*	0.1678880	1.0	1.0	—
3*d*	0.4509895	—	—	1.0

rameters of the DFT exchange (x) and correlation (c) nonlocality (GGA/LDA), respectively.

A proper choice and further reoptimization of the basis sets (BSs) presented in Tables I and II, which consists of the exponents (α_μ) and contraction coefficients (c_μ) for atom-centered Gaussian-type functions (GTFs), is another crucial point in the CRYSTAL calculations. For oxygen, we used the all-electron 8-411*sp*-1*d* BS with reoptimized outermost exponents (Table I). Small core Hay–Wadt pseudo-potentials (PP) [31] were used for core electrons with the BSs for both Ti (411*sp*-311*d*) and Sr (311*sp*-1*d*); their outermost shells were reoptimized more carefully (Table II). Optimization of all BSs was performed using the ParOptimize code [32], which implements the conjugated gradients optimization technique with a numerical computation of derivatives [33]. Fitting of the optimized BSs has been checked by calculating the lattice constant, bulk modulus, and elastic constants of $SrTiO_3$ bulk, as well as its band structure and other electronic properties [17]. The *F* centers and O vacancies were calculated by removing an oxygen atom as shown in Figure 1 and by either retaining or not in the vacancy the "ghost" wave function of O. The reciprocal space integration for models of the *F* center in $SrTiO_3$ (see section 2) has been performed with the suitable integer shrinking factors of two for both the Monkhorst–Pack and Gilat nets [34, 35].

3.2. VASP CALCULATIONS

The computational procedure of the VASP code [20, 36] includes an iterative solution of the Kohn–

TABLE II

Basis sets for outermost Ti and Sr orbitals constructed using Hay–Wadt small core pseudo-potentials [31].

	Ti				Sr			
		Contraction (c_μ)				Contraction (c_μ)		
Shell	Exponent (α_μ)	*s*	*p*	*d*	Exponent (α_μ)	*s*	*p*	*d*
1*s*		HAYWSC				HAYWSC		
2*sp*								
3*sp*	16.6627995	0.005288277	−0.002472365	—				
	3.82352098	0.348881629	−0.490787025	—				
	3.76734787	0.2	0.5	—				
	1.33437747	−0.846874184	0.047543445	—				
4*sp*	0.7725692	1.0	1.0	—	16.7295003	−0.040864984	0.006428855	—
					2.23218348	1.0	1.0	—
					1.98458795	9.26146754	−0.963768104	
5*sp*	0.4369296	1.0	1.0	—	0.6537827	1.0	1.0	—
6*sp*	—	—	—	—	0.2609586	1.0	1.0	—
3*d*	21.429541	—	—	0.088078981		HAYWSC		
	6.08722431	—	—	0.417373956				
	2.07945196	—	—	1.0				
4*d*	0.8310327	—	—	1.0	0.4699451	—	—	1.0
5*d*	0.3562744	—	—	1.0	—	—	—	—

Sham equations based on residual minimization and optimized charge-density mixing routines [37]. This includes calculation of the Hellmann–Feynman forces acting on the atoms and of the stresses on the unit cell [36]. The total energy is optimized with respect to the positions of the atoms within unit cell or supercell. The Kohn–Sham method employing a plane-wave basis set and the PP approximation is currently among the most successful techniques in computational materials science [38]. However, its formal simplicity demanded a price: first-row elements, transition metals, and rare-earth elements were found to be computationally time-consuming to treat with standard norm-conserving PPs [39]. Various attempts were made to generate more soft PPs: one of the most advanced approaches was the concept of ultrasoft pseudo-potentials (US-PP) introduced by Vanderbilt [40]. But its success is partly hampered by the difficulties in the construction of the pseudo-potentials, i.e., too many parameters (several cutoff radii) must be chosen and therefore extensive tests are required to obtain an accurate and highly transferable US-PP. Further development of this concept has been achieved by Blöchl [41] by a combining ideas from PP and linearized augmented plane-wave (LAPW) methods in a framework, called the projector augmented wave (PAW) method. Recently, the formalism of PAW method has been successfully implemented into the VASP code [20, 42], which allows users to combine it with the earlier implemented US-PP approach.

The VASP plane-wave calculations of the oxygen vacancy in the $SrTiO_3$ crystal (for the supercells described in Section 2) have been performed using the PAW PPs for the inner cores of all atoms [20, 42], while the kinetic energy cut-off (determining the whole set of plane waves with smaller energy included in the basis set) has been chosen as $E_{cut} = 415$ eV. The Monkhorst–Pack [34] ***k***-mesh $2 \times 2 \times 2$ has been employed for the energy evaluation with a density ranging from 0.04 to 0.51 $Å^{-1}$. The GGA-type exchange-correlation functional was chosen in the PW91 formulation [29]. The advantage of VASP plane-wave calculations [20] is that the complete optimization of lattice relaxation upon vacancy creation, even for large supercells, can be performed much faster than for CRYSTAL calculations based on the localized basis sets [19]. Geometry optimizations have been carried out with an accuracy 10^{-3} eV in the total energy. The electronic structure of defective $SrTiO_3$ perovskite calculated with both the CRYSTAL and VASP codes has been studied for the diamagnetic closed electronic shell (singlet) state, since we did not find any lower state employing spin polarized calculations [10].

4. Atomic and Electronic Structure of *F* Centers in a Cubic $SrTiO_3$ Crystal

Basic properties of a perfect cubic $SrTiO_3$ crystal calculated using the CRYSTAL code were analyzed in detail elsewhere [16, 17]. The lattice constant, a_o; bulk modulus, B; as well as elastic constants, c_{11}, c_{12}, and c_{44}, were obtained rather close to the experimental values (3.90 Å [43], 179 GPa [44], and 31.72 $\times$, 10.25 $\times$, and 12.35 $\times$ 10^{11} dyne/cm^2 [45], respectively) in almost all methods employed within the framework of the HF and DFT computational schemes. However, the parameters of the electronic structure were found to be quite sensitive to the method chosen. The best agreement with experimental results was obtained for the hybrid exchange technique (B3PW [30]) described in Section 3.1. Further improvement of the calculated optical gap was achieved by adding the d polarization orbital into the oxygen basis set (Table I): at the Γ point of the first BZ $\Delta\varepsilon^{\Gamma}_{gap} = 3.65$ eV, quite close to the experiment, 3.25 eV for the indirect bandgap [8]. The local properties of the electronic structure (charges and bond orders) for the perfect $SrTiO_3$ crystal obtained using the formalism of Wannier functions [16] have been considered above (Section 1).

When performing VASP-PAW calculations with the PW91 exchange-correlation functional, the structural parameters of cubic $SrTiO_3$ again were found to be quite reasonable: $a_o = 3.92$ Å and $B = 182$ GPa [10]. However, the optical bandgap of 2.59 eV is an evident underestimate, typical for this method [46]. Nevertheless, the new DFT + U method (U is the spherically averaged Hubbard parameter characterized as the Coulomb repulsion energy cost to place an extra electron on a particular site [47]), as recently implemented in the VASP code for both LDA and GGA approximations [20], allows one to avoid such an underestimate. When using this method, the DFT exchange-correlation functional is modified in such a way as to shift the lowest unoccupied level to higher energy, analogously to the hybrid DFT + HF method as implemented in the CRYSTAL code [19]. As a result, the DFT + U calculations could better describe the bandgap for the $SrTiO_3$(001) surface containing the F center [48].

TABLE III

Dependence of the nearest distance between *F* centers (d_{F-F}), formation energy of a single oxygen vacancy $E^{form}(F)$, and energy barrier $\Delta E^{diff}(F)$ of its (011) diffusion on both shape and size of supercell used for VASP calculations with 2 × 2 × 2 *k*-mesh.

Supercell	Extension	Type of lattice	d_{F-F} (Å)	$E^{form}(F)$ (eV)		$\Delta E^{diff}(F)$ (eV)
				Unrelaxed	Relaxed	
80-atom	$2\sqrt{2} \times 2\sqrt{2} \times 2\sqrt{2}$	fcc	11.04	9.00	7.73	0.41
135-atom	$3 \times 3 \times 3$	sc	11.71	9.17	7.89	0.35
160-atom	$2\sqrt{3} \times 2\sqrt{3} \times 2\sqrt{3}$	bcc	13.52	8.98	7.35	0.50
270-atom	$3\sqrt{2} \times 3\sqrt{2} \times 3\sqrt{2}$	fcc	16.56	8.98	7.17	0.38

4.1. OXYGEN VACANCY FORMATION AND MIGRATION

The formation energy of the *F* center in $SrTiO_3$ crystal was estimated as follows [10]:

$$E^{form}(F) = E(F) + E(O) - E(\text{perfect}), \qquad (6)$$

where $E(O)$ is the energy for the spin-polarized isolated oxygen atom (^3P state), and $E(F)$ and $E(\text{perfect})$ the energies of the defective and perfect crystals, respectively. A similar approach for the determination of $E^{form}(F)$ was used in Ref. [4]. In alternative approach [9, 11], the formation energies of the O vacancy were expressed via chemical potentials of O, Sr, and Ti atoms. However, the range of $E^{form}(F)$ calculated using both approaches for supercells of different shapes and sizes (6.5–8.5 eV, as noted in Section 1) is not so large as to give a preference to one of them when considering strontium titanate. Table III shows dependence of the vacancy formation energy in $SrTiO_3$ bulk on both supercell shape and size, which is accompanied by the large contribution coming from the lattice relaxation upon vacancy formation. The formation energy is reduced considerably (by 1.5–2.0 eV) when the positions of all atoms in the supercells are fully optimized. This demonstrates that the relaxation of even 14 nearest ions [neighboring Ti, O, and Sr coordination spheres directly shown in Fig. 1(a)] might be rather insufficient, and the inclusion of next-nearest coordination spheres is necessary (Table IV). Moreover, the lattice relaxation around the defect is periodically repeated in the supercell model, thus affecting the calculated total energy per cell: the larger the supercell, the smaller this artifact. We consider only $E^{form}(F)$ values estimated in VASP calculations, as complete optimization of the lattice relaxation in the large supercells is extremely time-consuming in the present version of the CRYSTAL code. The calculated defect formation energies mainly decrease with the increase of the supercell size, but they also depend on the shape of supercell (cf. the corresponding values for fcc 80-atomic and sc 135-atomic cells).

To calculate the energy barrier $\Delta E^{diff}(F)$ for oxygen vacancy diffusion using the VASP code (Table III), we consider a jump of the O atom from the eight possible sites nearest to the *F* center [Fig. 1(a)] toward the vacancy. We have estimated the saddle-point energy by fixing a hopping O atom at the middle of Sr-Ti-Sr triangle [Fig. 1(a)] crossed by oxygen migration trajectory, which has been (or was) found to be non-linear, while the rest of the lattice has been allowed to relax to the minimum of total energy. The $\Delta E^{diff}(F)$ (Table III) is sensitive to both the shape and size of the $SrTiO_3$ supercell; moreover, for optimized rhombohedric fcc and bcc supercells [Fig. 1(b, c)], the migration trajectories are not completely equivalent. Nevertheless, migration energies mainly decrease with the increase of the supercell size. Unfortunately, values of $E^{form}(F)$ and $\Delta E^{diff}(F)$ for the 4 × 4 × 4 supercell of 320 atoms could not be calculated due to computational limitation.

The sensitivity of calculated lattice relaxation around the defect to both supercell shape and size is also clearly seen in Table IV. For the same type of superlattice (sc, fcc, or bcc), expansion of the first coordination sphere (two Ti ions) is larger, whereas compression of the second sphere (eight O ions) is smaller with the increasing size of the supercell. However, the convergence of the lattice relaxation is complex, and a very low concentration of single *F* centers should be used to achieve it. For instance, fcc supercells are stretched along the *z*-axis and are compressed in the *xy*-plane [Fig. 1(b)]. This causes

TABLE IV

Dependence of lattice relaxation for the nearest equivalent atoms around single *F* center in a cubic $SrTiO_3$ crystal on both shape (Fig. 1) and size (Table III) of supercells (SCs) used in VASP calculations with 2 × 2 × 2 *k*-mesh.

Atoms nearest to *F* center	Unrelaxed distance from *F* center, a_o	Unrelaxed coordinates			No. of atoms shifted equivalently	Relative radial shifts δR_i from unrelaxed positions[a] (%)				
		x_i	y_i	z_i		80-atom SC, fcc	135-atom SC, sc	160-atom SC, bcc	270-atom SC, fcc	320-atom SC, sc
Ti	$a_o/2$	0	0	$\pm a_o/2$	2	7.21	7.16	7.08	8.28	7.76
O	$a_o/\sqrt{2}$	$\pm a_o/2$	0	$\pm a_o/2$	8	−7.59	−7.92	−7.98	−7.43	−7.79
		0	$\pm a_o/2$	$\pm a_o/2$						
Sr	$a_o/\sqrt{2}$	$\pm a_o/2$	$\pm a_o/2$	0	4	3.51	3.48	3.45	3.42	3.94
O	a_o	$\pm a_o$	0	0	4	3.16	2.98	2.49	2.87	3.56
		0	$\pm a_o$	0						
O	a_o	0	0	$\pm a_o$	2	−1.72	−1.56	−1.67	−1.05	−1.28

[a] Positive shift corresponds to expansion of the atomic coordination sphere, whereas negative sign means its compression.

the larger *z*-shifts of Ti ions nearest to the O vacancy in 80- and 270-atomic fcc supercells, as compared with 135- and 320-atomic cubic supercells (Table IV), whereas *xy*-shifts of the nearest O and Sr ions are smaller in the former case. Nevertheless, the range of δR_i for equivalently shifted atoms in equidistant supercells of different shapes and sizes is small enough (≤1.0%) to suggest the stabilization of a single O vacancy in a cubic $SrTiO_3$ crystal when using large equidistant supercells containing 270 and 320 atoms. When trying to use the CRYSTAL code for partial optimization of the total energy for the same supercells, we obtained a markedly smaller expansion of the first coordination sphere involving the two nearest titanium ions as compared with VASP complete optimization (1.5–2% vs. 7–8%). The same is true for the next-nearest coordination spheres, an additional argument in favor of the VASP optimization.

4.2. INFLUENCE OF OXYGEN VACANCIES ON THE ELECTRONIC PROPERTIES

To gain deeper insight into the defective $SrTiO_3$ bulk from the CRYSTAL calculations on different superlattices described in Section 2, we have analyzed its electronic structure. Redistribution of the electron density due to O vacancy formation is shown in Figure 2(a, b) as calculated for the equidistant fcc supercells with different extensions. In both plots, the Mulliken electron charge (1.1–1.3 *e*) is localized within a neutral O vacancy; in other words, 0.6–0.8 *e* is equally divided by the two Ti ions nearest to the neutral *F* center and mainly localized on their $3d(z^2)$ orbitals, making the largest contribution to the defect bands shown in Figure 3(a, b). Figure 2 clearly demonstrates the effect of size of the same fcc-type supercell, with $2\sqrt{2} \times 2\sqrt{2} \times 2\sqrt{2}$ and $3\sqrt{2} \times 3\sqrt{2} \times 3\sqrt{2}$ extensions, on localization of the charge redistribution. For the 80-atom supercell, mutual interaction of the neighboring O vacancies is clearly seen, especially along the –Ti–O–Ti– axes, whereas for the 270-atom supercell, the more-or-less visible redistribution of the electron density is limited by a region of ±1.5–2.0 a_o around a vacancy, in the *z*-direction.

As mentioned earlier, the VASP code [20] is markedly more efficient than the CRYSTAL code for optimization of the lattice relaxation around a vacancy [19]. However, the latter possesses a noticeable advantage when describing the electronic properties of defective crystals. For instance, remaining "ghost" orbitals localized at the position of

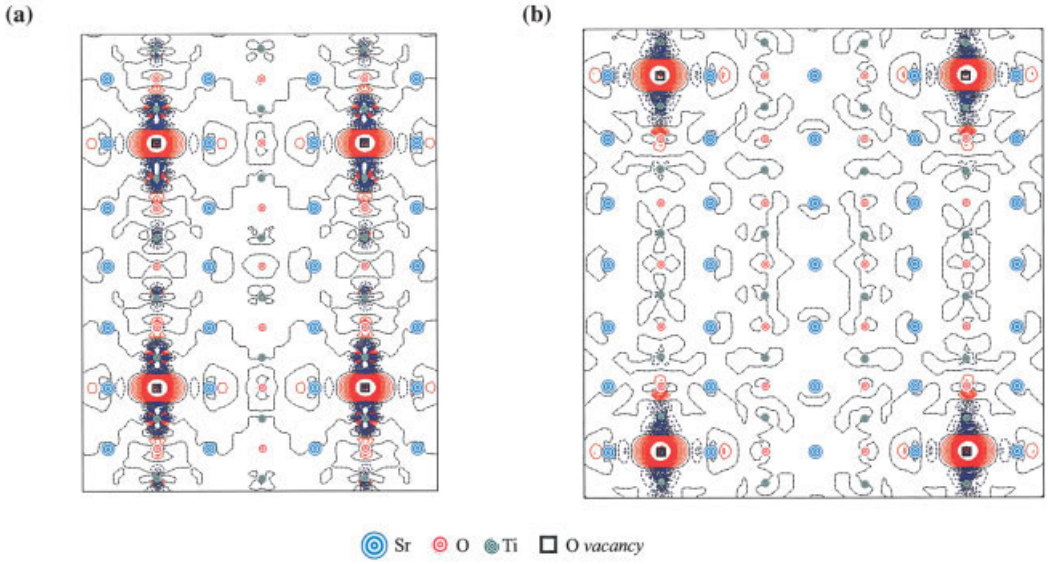

FIGURE 2. Two-dimensional (2D) difference electron density maps $\Delta\rho(\mathbf{r})$ (the total density in the perfect $SrTiO_3$ bulk minus the sum of electron densities of both isolated oxygen atoms and defective $SrTiO_3$) projected onto the (110) section plane *P–P* [Fig. 1(b)] for 80-atom (a) and 270-atom (b) fcc supercells containing a single oxygen vacancy. Dash-dot isolines correspond to the zero level. Solid and dash isolines describe positive and negative values of electron density, respectively. Isodensity increment is 0.002 *e* $Å^{-3}$.

removed atom allow us to calculate the defect energy band within the optical gap (Fig. 3). The defect–defect interaction is also manifested in the CRYSTAL–B3PW calculations through the finite defect bandwidth. The defect bands cannot be directly studied using the VASP code, whereas calculations using the PW91 functional strongly underestimate the $SrTiO_3$ optical bandgap, as noted earlier.

According to our CRYSTAL–B3PW calculations on $SrTiO_3$ superlattices with the centered oxygen vacancy [Table V and Fig. 3(a, b)], the *F* center energy level in the bandgap approaches the conduction band bottom (being separated by $\Delta\varepsilon^{\Gamma}_{db\text{-gap}}$ from it), moving from 0.69 eV for the 80-atom supercell (with a bandwidth of 0.15 eV), down to 0.57 eV (0.08 eV) for 160 atoms, and finally reaching the optical ionization energy of 0.49 eV (almost neglect-

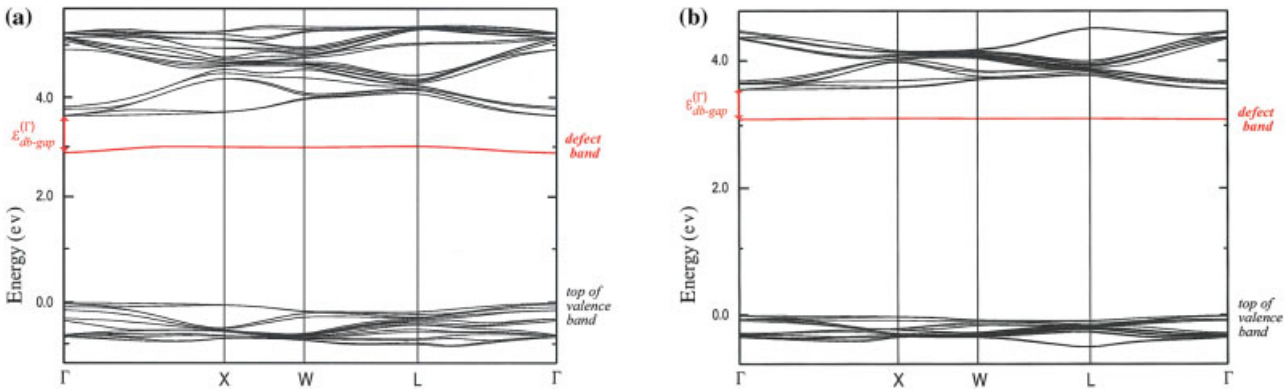

FIGURE 3. Band structure of unrelaxed $SrTiO_3$ crystal with a single *F* center per fcc supercell containing either 80 atoms (a) or 270 atoms (b). Energy bands corresponding to the *F* center are split off the conduction bands. Their depth (gap) relative to the bottom of the conduction band at the Γ point is $\Delta\varepsilon^{\Gamma}_{db\text{-gap}}$.

TABLE V

Dependence of the *F* center energy level position with respect to the conduction band bottom of unrelaxed $SrTiO_3$ crystal with periodically distributed oxygen vacancies ($\Delta\varepsilon^{\Gamma}_{db\text{-gap}}$ shown in Fig. 3), its dispersion ($\delta\varepsilon_{db\text{-gap}}$), and distance between the nearest *F* centers ($d_{F\text{–}F}$) as a function of the supercell size used in CRYSTAL–B3PW calculations with 2 × 2 × 2 *k*-mesh.*

Supercell	Extension	Type of lattice	$d_{F\text{–}F}$ (Å)	$\Delta\varepsilon^{\Gamma}_{db\text{-gap}}$ (eV)	$\delta\varepsilon_{db\text{-gap}}$ (eV)
80-atom	$2\sqrt{2} \times 2\sqrt{2} \times 2\sqrt{2}$	fcc	11.04	0.69	0.15
135-atom	$3 \times 3 \times 3$	sc	11.71	0.72	0.23
160-atom	$2\sqrt{3} \times 2\sqrt{3} \times 2\sqrt{3}$	bcc	13.52	0.57	0.09
270-atom	$3\sqrt{2} \times 3\sqrt{2} \times 3\sqrt{2}$	fcc	16.56	0.49	0.02
340-atom	$4 \times 4 \times 4$	sc	15.61	0.49	0.03

* The defect level position is calculated at the Γ point of the first Brillouin zone.

ing the dispersion of 0.02–0.03 eV) for 270 and 320 atoms where the distance between the nearest defects is close to four lattice constants. Note that the commonly believed experimental estimate of the *F* center ionization energy is much smaller [18]. Achieving the convergence with the supercell increases up to 270–320 atoms, the defect–defect interaction becomes negligible, thus approaching a realistic model of a single *F* center, similar to the study of the Fe impurities in $SrTiO_3$ [21].

The results presented in Table V confirm that the 135-atom supercell is not big enough to reduce defect–defect interactions; its dispersion ($\delta\varepsilon_{db\text{-gap}}$) is even larger than for an 80-atom supercell with a different shape, i.e., $\delta\varepsilon_{db\text{-gap}}$ is sensitive to both the shape and size of the equidistant supercell, similar to other properties described before. At the same time, the defect band for the 270-atom supercell [Fig. 3(b)] is almost a straight line. Table V clearly shows that the use of both supercells of 270 and 320 atoms practically eliminates the interaction between periodically distributed point defects, confirming the analogous conclusion made before, analyzing the electron charge redistributions around oxygen vacancies [Fig. 2(a, b)].

5. Summary

We have analyzed the convergence of periodic defect calculations to the limit of the single oxygen vacancy. To obtain converged values for the atomic structure, formation, and migration energies of O vacancy, as well as the electronic properties corresponding to a single *F* center in $SrTiO_3$ bulk, the large equidistant supercells containing at least 270 atoms ($d_{F\text{–}F} \geq 4a_o$) are required when performing DFT calculations on defective perovskites. This study confirms several conclusions based on our recent HF calculations on the Fe impurities in $SrTiO_3$ bulk [21]. Equidistant supercells with extensions $3\sqrt{2} \times 3\sqrt{2} \times 3\sqrt{2}$ (270 atoms) and $4 \times 4 \times 4$ (320 atoms) necessary for a correct description of single oxygen vacancies in strontium titanate markedly surpass supercells containing 40–135 atoms used in most previous first-principles simulations [4, 10–13]. The results obtained in those studies should be critically analyzed to avoid wrong conclusions about the nature of *F* centers in perovskites.

Our VASP calculations with complete optimization of lattice relaxation around the *F* centers give 7.1 eV as a reasonable estimate for the vacancy formation energy $E^{\text{form}}(F)$ and 0.4–0.5 eV for their migration barrier $\Delta E^{\text{diff}}(F)$ at low vacancy concentration. The vacancy formation energy cannot be directly measured experimentally, whereas the experimental estimate for the barrier of diffusion energy is noticeably larger: 0.86 eV [6]. CRYSTAL–B3PW calculations on the electronic properties of a single *F* center in the unrelaxed (or partially relaxed) $SrTiO_3$ lattice show the formation of a defect band below the conduction band bottom, which is mainly composed of $3d(z^2)$ orbitals of the two nearest Ti ions. Its separation $\Delta\varepsilon^{\Gamma}_{db\text{-gap}}$ from the conduction band bottom approaches 0.49 eV, with a negligible dispersion $\delta\varepsilon_{db\text{-gap}}$ of the bandwidth (0.02–0.03 eV) for both 270- and 320-atom supercells. Redistribution of the electronic charge around oxygen vacancies remains well localized even in large supercells, when the interaction between homogeneously distributed point defects is practically eliminated. However, CRYSTAL recalculations of the *F* centers using the VASP-optimized geome-

try substantially affect the electronic structure. More careful study of this effect is necessary.

The present study clearly demonstrates the advantage of combining the VASP plane-wave calculations [20] with the CRYSTAL calculations based on the localized basis sets [19]. The former is necessary for the complete optimization of both lattice relaxation upon vacancy creation (even for large supercells) and its migration, whereas the latter allows one to study in more detail the electronic structure for both unrelaxed and relaxed lattice.

ACKNOWLEDGMENTS

This study was partly supported by the MRSEC program of the National Science Foundation (DMR-0076091) at the Materials Research Center of Northwestern University, Evanston, Illinois (to E. K. and Y. Z.). The technical assistance of Yu. Mastrikov and S. Piskunov was most valuable. The authors kindly thank J. Carrasco, D. E. Ellis, E. Heifets, F. Illas, L. N. Kantorovich, N. Lopez, J. Maier, and D. Wolf for fruitful discussions.

References

1. Muller, D. A.; Nakagawa, N.; Ohtomo, A.; Grazul, J. L.; Hwang, H. Y. Nature 2004, 430, 657.
2. Cox, P. A. Transition Metal Oxides; Clarendon Press: Oxford, UK, 1995.
3. Smyth, D. M. Annu Rev Mater Sci 1985, 15, 329.
4. Astala, R.; Bristowe, P. D. Model Simul Mater Sci Eng 2001, 9, 415.
5. Szot, K.; Speier, W.; Carius, R.; Zastrow, U.; Beyer, W. Phys Rev Lett 2002, 88, 075508.
6. Denk, I.; Munch, W.; Maier, J. J Am Ceram Soc 1995, 78, 3265.
7. Adachi, Y.; Kohiki, S.; Wagatsuma, K.; Oku, M. Appl Surf Sci 1999, 143, 272.
8. Van Benthem, K.; Elsaesser, C.; French, R. H. J Appl Phys 2001, 90, 6156.
9. Buban, J. P.; Iddir, H.; Ogut, S. Phys Rev B 2004, 69, 180102(R).
10. Carrasco, J.; Illas, F.; Lopez, N.; Kotomin, E. A.; Zhukovskii, Yu. F.; Piskunov, S.; Maier, J.; Hermansson, K. Phys Status Solidi C 2005, 2, 153.
11. Tanaka, T.; Matsunaga, K.; Ikuhara, Y.; Yamamoto, T. Phys Rev B 2003, 68, 205213.
12. Donnenberg, H.-J. Atomic Simulations of Electro-Optical and Magneto-Optical Materials; Springer Tracts in Modern Physics; Vol. 151; Springer: Berlin, 1999.
13. Ricci, D.; Bano, G.; Pacchioni, G.; Illas, F. Phys Rev B 2003, 68, 224105.
14. Akhtar, M.; Akhtar, Z.; Jackson, R. A.; Catlow, C. R. A. J Am Ceram Soc 1995, 78, 421.
15. Crawford, J.; Jacobs, P. W. M. J Solid State Chem 1999, 144, 423.
16. Usvyat, D. E.; Evarestov, R. A.; Smirnov, V. P. Int J Quantum Chem 2004, 100, 352.
17. Piskunov, S.; Heifets, E.; Eglitis, R. I.; Borstel, G. Comput Mater Sci 2004, 29, 165.
18. Moos, R.; Haerdtl, K.-H. J Am Ceram Soc 1997, 80, 2549.
19. Saunders, V. R.; Dovesi, R.; Roetti, C.; Orlando, R.; Zicovich-Wilson, C. M.; Harrison, N. M.; Koll, K.; Civalleri, B.; Bush, I. J.; D'Arco, Ph.; Llunell, M. CRYSTAL-2003 User Manual; University of Turin: Turin, Italy, 2003.
20. Kresse, G.; Hafner, J. VASP Guide; University of Vienna: Vienna, Austria, 2003.
21. Evarestov, R. A.; Piskunov, S.; Kotomin, E. A.; Borstel, G. Phys Rev B 2003, 67, 064101.
22. Evarestov, R. A.; Smirnov, V. P. J Phys: Condens Matter 1997, 9, 3023.
23. Evarestov, R. A. Phys Status Solidi A 2005, 202, 235.
24. Pisani, C.; Dovesi, R.; Roetti, C.; Causá, M.; Orlando, R.; Casassas, S.; Saunders, V. R. Int J Quantum Chem 2000, 77, 1032.
25. Bredow, T.; Evarestov, R. A.; Jug, K. Phys Status Solidi B 2000, 222, 495.
26. Makov, G.; Shach, R.; Payne, M. C. Phys Rev B 1996, 53, 15513.
27. Piskunov, S.; Heifets, E.; Kotomin, E. A.; Maier, J.; Eglitis, R. I.; Borstel, G. Surf Sci 2005, 575, 75.
28. Becke, A. D. Phys Rev A 1988, 38, 3098.
29. Perdew, J. P.; Wang, Y. Phys Rev B 1992, 45, 13244.
30. Becke, A. D. J Chem Phys 1988, 98, 5648.
31. Hay, P. J.; Wadt, W. R. J Chem Phys 1984, 82, 270 (I); 284 (II); 299 (III).
32. Heifets, E.; Eglitis, R. I.; Kotomin, E. A.; Maier, J.; Borstel, G. Phys Rev B 2001, 64, 235417.
33. Press, W. H.; Teukolsky, S. A.; Vetterling, W. T.; Flannery, B. P. Numerical Recipes in Fortran 77; Cambridge University Press: New York, 1997.
34. Monkhorst, H. J.; Pack, J. D. Phys Rev B 1976, 13, 5188.
35. Gilat, G. Phys Rev B 1982, 26, 2243.
36. Kresse, G.; Hafner, J. Phys Rev B 1993, 48, 13115; 1994, 49, 14251.
37. Kresse, G.; Furthmüller, J. Comput Mater Sci 1996, 6, 15; Phys Rev B 1996, 54, 11169.
38. Singh, D. J. Planewaves, Pseudopotentials and the LAPW Method; Kluwer Academic: Norwell, 1994.
39. Hamann, D. R.; Schlüter, M.; Chiang, C. Phys Rev Lett 1979, 43, 1494; Bachelet, G. B.; Schlüter, M.; Chiang, C. Phys Rev B 1982, 26, 4199.
40. Vanderbilt, D. Phys Rev B 1990, 41, 7892.
41. Blöchl, P. E. Phys Rev B 1994, 50, 17953.
42. Kresse, G.; Joubert, D. Phys Rev B 1999, 59, 1758.
43. Abramov, Yu. A.; Tsirelson, V. G.; Zavodnik, V. E.; Ivanov, S. A.; Brown, I. D. Acta Crystallogr B 1995, 51, 942.
44. Hellwege, K. H.; Hellwege, A. M., Eds. Ferroelectrics and Related Substances; Landolt-Börnstein, New Series, Group III; Springer-Verlag: Berlin, 1969; Vol 3.
45. Bell, R. O.; Rupprecht, G. Phys Rev 1963, 129, 90.
46. Moreira, I. P. R.; Illas, F.; Martin, R. L. Phys Rev B 2002, 155102.
47. Rohrbach, A.; Hafner, J.; Kresse, G. J Phys Condens Matter 2003, 15, 979.
48. Fang, Z.; Terakura, K. Surf Sci 2000, 479, L65.